# Flux lattice and vortex structure in $2H$-$NbSe_2$ in inclined fields

H. F. Hess, C. A. Murray, and J. V. Waszczak
*AT&T Bell Laboratories, 600 Mountain Avenue, Murray Hill, New Jersey 07974-0636*
(Received 6 April 1994)

The structure's of the flux-line lattice and of individual vortices on the surface of a uniaxial anisotropic superconductor $2H$-$NbSe_2$ are studied for arbitrary magnetic fields using the scanning tunneling microscope. The basis vectors show a distortion consistent with bulk anisotropic London theory, however, their angular orientation with respect to the tilt direction differs by about 30° from that predicted. Various lattice-buckling instabilities are observed when the field is inclined more than 80° away from the $c$ axis. The star-shaped structure of the core distorts into a spiky comet shape as the field is tilted into the plane. If the field is along the surface (perpendicular to the $c$ axis), evenly spaced parallel streaks reveal the subsurface vortex spacing.

## INTRODUCTION

The structure of the flux-line lattice in anisotropic superconductors has long been the subject of experimental and theoretical study. The source of the flux lattice anisotropy is an anisotropic Fermi surface, which can be characterized by an effective-mass tensor. That this can deform the flux-line lattice was established theoretically[1,2] and experimentally[3] for modestly anisotropic Technitium (mass ratio $m_c/m_a \sim 0.7$) in early neutron-scattering experiments. The much larger mass ratios (55 for Y-Ba-Cu-O and 3600 for Bi-Sr-Ca-Cu-O) of the oxide high-$T_c$ superconductors sparked renewed theoretical and experimental interest in the flux-line lattice structure. Oval vortices and highly anisotropic flux lattices were seen in Y-Ba-Cu-O by Bitter decoration[4] experiments. At low fields vortex chains have recently been proposed[5] and observed in Bi-Sr-Ca-Cu-O (Ref. 6) and Y-Ba-Cu-O.[7] A complex combination of hexagonal lattice and vortex chains is observed in the more anisotropic Bi-Sr-Ca-Cu-O, with Bitter decoration experiments. For higher fields ($H_{c1} < H < H_{c2}$) applied at arbitrary angle to the anisotropy axis, further detailed predictions regarding the distortion and angular order have been made on the basis of anisotropic London theory[8] and anisotropic Landau-Ginzberg theory.[9] With the exception of a few neutron-scattering measurements[3,10,11] there has been no systematic effort to explore this regime under a variety of fields strengths and field directions on moderately anisotropic superconductors, and test the conditions under which the theories are valid.

In this article we summarize comprehensive measurements of the flux-line lattice structure and vortex core structure in uniaxial anisotropic superconductors when the magnetic field is inclined with respect to the $c$ axis of the sample. Part of these results were reported earlier.[12] We also compare with recent neutron-scattering[13] and decoration experiments[14] on the same compound. We study the conventional anisotropic layered superconductor $2H$-$NbSe_2$. It has a transition temperature $T_c$ of 7.2 K, a mass ratio[15] $m_c/m_a \sim 11$, and an in-plane penetration depth $\lambda$ of 0.2 $\mu$m,[16] and is considered a clean superconductor. The very low critical current of $J_c \sim 30$ A/cm$^2$ of this material insures the minimal role of pinning in describing the lattice structures. We will focus on the flux-line lattice that forms at intermediate fields, when its lattice spacing in the $ab$ plane, $a_0$, is comparable to or smaller than the magnetic penetration depth $\lambda$. Images of the vortex core shape in inclined fields are also presented and compared to previous measurements[17] when the field was normal. We find (1) a lattice distortion by an amount that is quantitatively predicted by anisotropic Landau-Ginzberg theory when $a_0/\lambda < 1$; (2) a lattice that appears less stretched and more isotropic if $a_0/\lambda \sim 1$; (3) an angular orientation of the lattice that is at odds with the same theory at all angles and field strength; (4) at higher angles, a lattice buckling at various periods showing mostly $2\times1$, and sometimes $3\times1$ or even $4\times1$ superlattice unit cells; (5) a distortion of the structure of the vortex core, which transforms from a symmetric star shape with perpendicular field to a spiky comet shape at inclined magnetic fields; and (6) an observation of evenly spaced streaks for fields parallel to the surface that may reflect a yet more dense subsurface vortex spacing.

## EXPERIMENTAL DETAILS AND STM DATA

The magnetic fields were applied by a three-axis superconducting magnet. The direction of the applied magnetic field is indicated in the schematic of the sample geometry in Fig. 1. The applied field of magnitude $H_a$ is inclined away from the $c$ axis by an angle $\theta$. The in-plane component of the magnetic field is oriented at an angle $\varphi$ away from one of the $\Gamma M$ crystalline directions. The $\Gamma M$ direction corresponds also to the charge density wave-vector direction of this compound and is rotated 30° from the crystalline **a** axis. About 100 different field configurations were explored at four different field magnitudes [$H_a = 0.5, 1.0, 2.25, 5.0$ kG, where the hexagonal Abrikosov Lattice spacing $a_0 = (2\Phi_0/\sqrt{3}B)^{1/2}$ would be $1.1\lambda$, $0.77\lambda$, $0.52\lambda$, and $0.35\lambda$], at ten different values of $\theta$, and at two different planar projections $\varphi = 7°$ and $-21°$. A second sequence at 5.0-kG field focuses on the

 

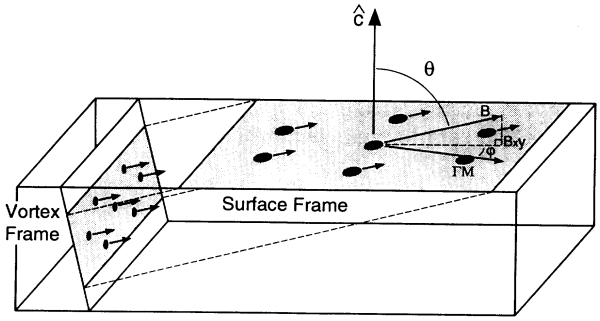


FIG. 1. Schematic detail of the direction of the magnetic field, the crystalline orientation, the scanned surface and the plane of the vortex basis vectors.

shallow tilt ($\theta=78°-90°$) behavior at $\varphi=1°$ and $-29°$. The sample was heated above $T_c$ and field cooled for each new magnetic-field configuration.

The $NbSe_2$ is cleaved in air and has dimensions of roughly 0.3 cm×0.3 cm×50 $\mu$m. It is mounted on the scanning tunneling microscope (STM) which has a PtIr tip, and cooled in vacuum to 0.2 K by a dilution refrigerator. Most lattice measurements were performed at a tunneling current of up to 10 pA with a tip-sample bias dc voltage of 1.3 mV. This value is just above the energy gap for 2H-$NbSe_2$ and is the point of maximum differential conductance in the spectra. Near the core this conductance is 40% lower.[17] For reference a $dI/dV$ spectra of the superconducting region is shown in the inset of Fig. 2 with the arrow indicating the measured differential conductance. This differential conductance is monitored by applying an additional small ac voltage $\sim 0.1$ mV (for lattice images) between the tip and sample and monitoring the ac current response with a lock-in amplifier. The magnitude of the conductance is recorded while scanning the tip in a raster pattern over a 1.4 $\mu$m×1.4 $\mu$m or a 2.1 $\mu$m×2.1 $\mu$m area on the surface. A grey scale image then shows the superconducting regions with an enhanced conductance as white and the cores with a lower conductance as dark.[17]

The resulting conductance images are collected in Fig. 2. The same physical area on the sample was used in all of the images. The direction of the in-plane field projection and $\Gamma M$, determined from the atomic scale lattice images, are indicated. A simple hexagonal Abrikosov lattice is observed when $\theta\sim 0°$ and the field is normal to the surface. We always observe the same angular orientation of this flux lattice since it is locked to the underlying crystalline lattice. Higher magnification STM images of the atomic lattice show the direction of $\Gamma M$ and indicate that the crystalline **a** direction (the atomic lattice **a** direction is 30° from $\Gamma M$) is identical to the nearest-neighbor vortex direction.[17]

One can see in Fig. 2, that the vortex lattice on the surface of the sample gradually stretches in the direction of the field inclination, as the field direction is rotated away from normal to the sample: the larger the tilt, the greater the stretching. In addition to this stretching there is also a dilation in the other perpendicular direction, as well as a twisting of the angular orientation of the lattice towards the applied field direction.

## ANALYSIS OF THE BASIS VECTORS

In order to evaluate the stretching and twisting of the flux-line lattice quantitatively, we extract the basis vectors from the STM images. Several steps are involved. First, the location $r_i$ of the $i$th vortex is determined by fitting the conductance depressions to Gaussians of revolution and evaluating their centers. For the 256×256 pixel$^2$ images each vortex can be determined to 0.5 pixel accuracy. To determine a particular nearest-neighbor vector, we simply plot all of the vectors connecting the neighbors $(r_i-r_j)$ or the pair-correlation function of the vortices. Figure 3 shows such reduced data for $B=2.25$ kG and $\varphi=7°$. The six nearest-neighbor vectors from six clouds of points, labeled by $l$, that are spaced by about 60° if the field is normal to the surface. The center of each cloud defines the averaged basis vectors $\mathbf{r}_l^{nn}$:

$$\mathbf{r}_l^{nn}=(1/N)\sum(\mathbf{r}_i-\mathbf{r}_j)\ ,$$

where $N$ is the number of points and the sum is over all pairs of points in the image.

Several small corrections must be made to these basis vectors to better evaluate the actual flux-line lattice vectors: (1) The residual linear $x,y$ spatial distortions of the microscope are determined by comparing the six nearest-neighbor vectors, when the field is normal, with an ideal hexagonal arrangement. Any deviation of these six data vectors from the ideal hexagonal arrangement is used to determine the residual linear $x,y$ spatial distortions of the microscope. With these 5% corrections we determine vortex positions to about 1% accuracy for other arbitrary field orientations. (2) Another correction is to account for any misalignment of the direction of the sample $c$ axis $\theta_c$ with the magnet $z$ axis $\theta_H$. This is done to a 0.2° accuracy simply by checking the vortex density. The number of vortices per area should scale as $H_z=H\cos(\theta_H-\theta_c)$ at the highest fields (5 kG), where demagnetization factors and anisotropy corrections are negligible. If we require the density to scale with $H_z$ then the misalignment angle is evaluated at $\theta_c=-1.1°\pm 0.2°$ for both $\varphi=7°$ and $\varphi=-21°$. The tilt angle of the applied field with respect to the $c$ axis is then defined to be the applied angle $\theta_a=\theta_H-\theta_c$. (While this correction may seem small it will have important consequences in determining effective mass and is the direct reason why the evaluated effective mass is about 20% larger in this article compared to our previous article[12] where this correction was neglected.)

The average position of each of the six clouds of nearest-neighbor points is evaluated, then corrected for the instrumental distortions and labeled with the proper tilt angle. Those vectors are then rotated by 15.6° so that $\Gamma M$, is horizontal, normalized by $a_0$, and replotted in the upper sections labeled surface frame in Fig. 4 for $\varphi=7°$ and Fig. 5 for $\varphi=-21°$. The four parts of these figures labeled *a*, *b*, *c*, and *d* correspond to the four applied fields. In the surface frame the six basis vectors lie equally

spaced on a circle for normal fields, and on an ellipse that has a semimajor axis that aligns with the in-plane field projection at finite tilt. The sequence of different symbols in each figure show the evolution of the basis vectors for different magnetic field tilt angles.

Instead of analyzing the data in these corrected surface coordinates, $x$ and $y$, we make another transformation to the vortex lattice coordinates $x'$ and $y'$ with $z' \| B$, to simplify the connection with theory. In Figs. 4 and 5, these are the bottom subplots labeled "vortex frame." Figure 1

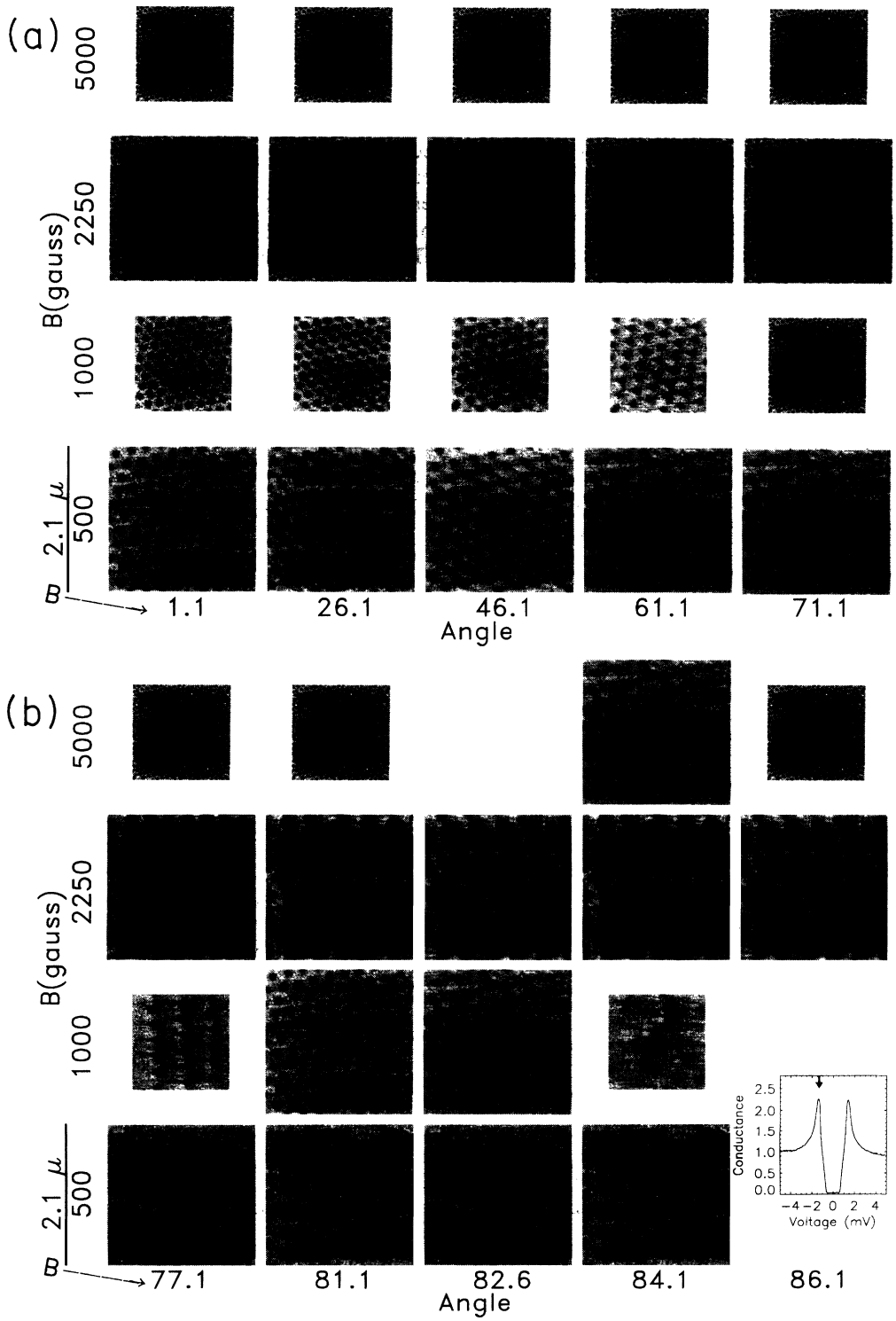


FIG. 2. Raw STM data showing on a grey scale the differential conductance $dI/dV(x,y)|_V$ at a dc voltage of 1.3 mV, just above the superconducting gap. (Zero-field spectrum is indicated in the inset.) The dark spots correspond to vortices where the differential conductance is reduced. Tilt angles, directions, and field magnitude are indicated.

shows its relationship to the surface frame. At high fields this transformation is very well approximated to $<0.1°$ accuracy by a $\cos\theta_a$ multiplication of the vector components along the $B_{xy}$ direction. At lower fields $\sim 500$ G the direction of induction $B$ can deviate from the direction of the applied field $H_a$ by up to 1°. This is a consequence of mass anisotropy and can be estimated for a slab geometry[18] (demagnetization factor of 1):

$$\tan(\theta)-\tan(\theta_a)+\frac{B_0}{H\cos(\theta_a)}\frac{\sin(\theta)}{\sqrt{1+\varepsilon\cos(\theta)}}=0\ , \qquad (1)$$

where

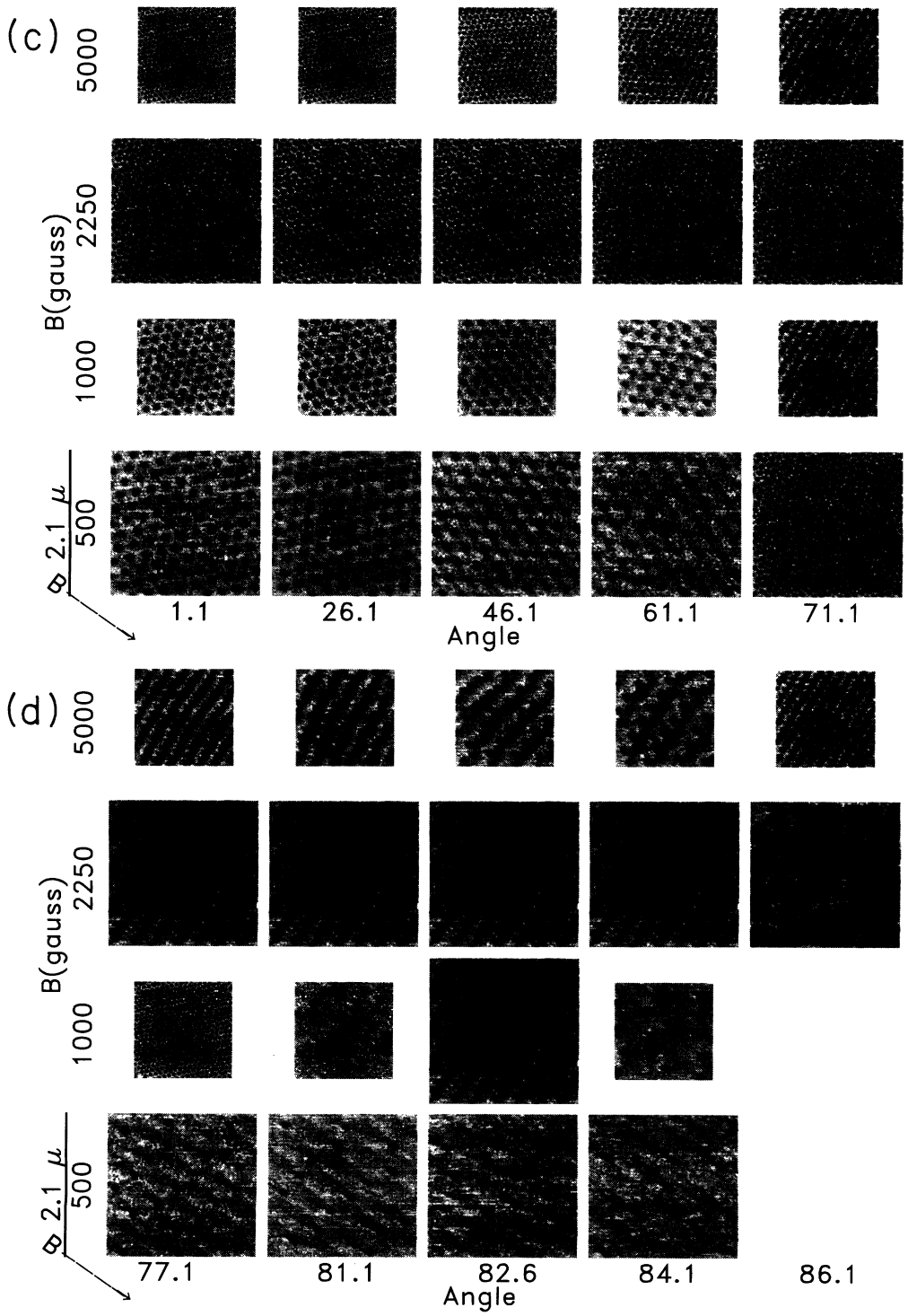


FIG. 2. (*Continued*).

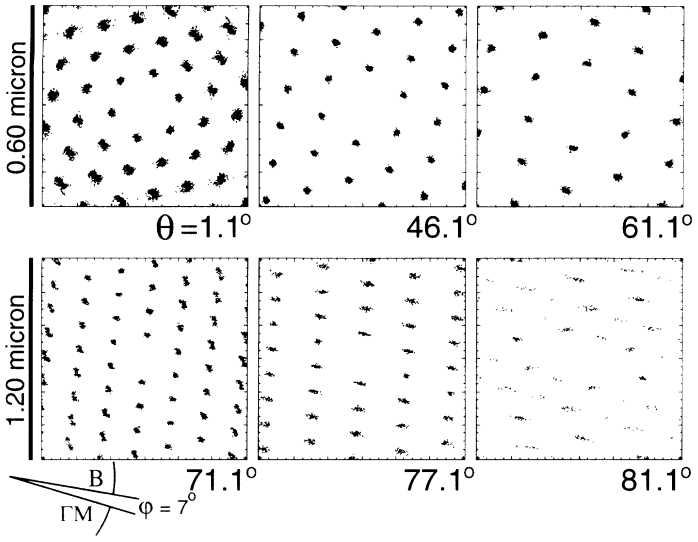


FIG. 3. A real-space plot showing the locations and distributions of the nearest-neighbor vortex basis vectors $r_{ij}$, for six of the images of Fig. 2. In each image of the six clouds of points are each averaged to obtain the representative basis vectors.

$$B_0=\frac{\Phi}{4\pi\lambda_c\lambda_{ab}}\ln\left[\beta\frac{H_c}{H}\right] . \quad (2)$$

We use this correction with $\varepsilon=m_c/m_a-1=10$ in replotting the basis vectors in lattice coordinates. The labels $\theta_a$ however still refers to the angle between $c$ and the applied field $H_a$, while $\theta$ is the angle between c and the induction $B$.

## FLUX LATTICE DISTORTION

### Real-space correlation length

A quantitative measure of the perfection of the flux lattice is given by the radial correlation length $\xi$. This is analyzed for the perpendicular fields ($\theta=1.1°$) at the four magnetic fields. Typically we find that our ability to measure it is limited by the finite number of vortices in the scan area. This is the case for the 500- and 1000-G data, where the respective lower bounds of $3a_0$ and $5a_0$ can be placed on $\xi$. Better bounds can be placed with the higher field conditions, of 2250 and 5000 G. The 5000-G data is shown in real space, Fig. 6 (left), along with the associated radial correlation function $g(r)$ plotted as a solid line in Fig. 6 (right), and the fit with $\xi=19a_0\pm2a_0$ plotted as a dotted line. Again, this correlation length is a lower bound limited by the image size. For the 2250-G data we find the correlation length is not resolution limited by the finite image size, but rather is determined by the occasional line dislocation that sometimes appears in our images. Two such dislocations in the 2250-G data reduce its length to $5a_0$. This suggests that for zero or small tilt angles the flux lattice correlation length is limited mainly by the line dislocation density.

### Ellipse formation

Now that the lattice basis vectors have been determined in the vortex frame, the flux lattice distortion can be measured. This is accomplished by fitting the six basis vectors (transformed to the vortex frame) to an ellipse. For normal fields $\theta=0°$ the vectors all lie on a circle. If the material were isotropic and surface effects are assumed unimportant, this circular pattern should persist independent of field angle in the vortex frame. Instead we find the basis vectors lie on an ellipse where the semiminor axis of radius $\gamma$ is aligned with the $c$-axis projection, in agreement with simple bulk London[8] or Landau-Ginzberg[9] theories. This alignment between the fitted ellipse axis and the $c$-axis projection is accurate to within experimental error for all angles and applied field magnitudes. This ranges from $\pm10\%$ at 26°, worst case, to $\pm1\%$ at 80°, best case. The circles and ellipses for $\theta_a=1.1°$ and $\theta_a=71.1°$ data are plotted in Figs. 4 and 5 as a guide.

The angle dependence of the ellipse fitting parameter (semimajor radius $1/\gamma$) is collected in Figs. 7 and 8 for the two in-plane projections $\varphi=7°$ and $-21°$. It is plotted vs the angle $\theta$ between the $c$ axis and the induction which is slightly different from $\theta_a$ used earlier. We see that $1/\gamma$ increases smoothly with tilt angle. The bulk London[8] or Landau-Ginzberg[9] theories predict the semiminor axis length as a function of tilt angle to be

$$\gamma(\theta)=\left[1+\frac{m_a}{m_c}\tan^2(\theta)\right]^{1/4}\cos^{1/2}(\theta) . \quad (3)$$

The solid dashed and dotted lines show the angle dependence of $\gamma$ for Eq. (3) with the indicated mass ratios. A one parameter fit gives a value of $m_c/m_a$ that approaches 11 at the highest fields of 5 kG. This is consistent with independent measurements[15] of $m_c/m_a\sim11$ by $H_{c2}$ anisotropy. From this we conclude good agreement with simple anisotropic London or Landau-Ginzberg theories at 5.0 kG where $a_0/\lambda\sim0.3$. Very recently small-angle neutron-scattering measurements[13] at 8 kG on $2H$-$NbSe_2$ have shown the same behavior with a fitted mass ratio of $10.1\pm0.9$. Since the STM reveals the surface vortex positions and neutron-scattering probes the bulk, the agreement shows that there is no significant

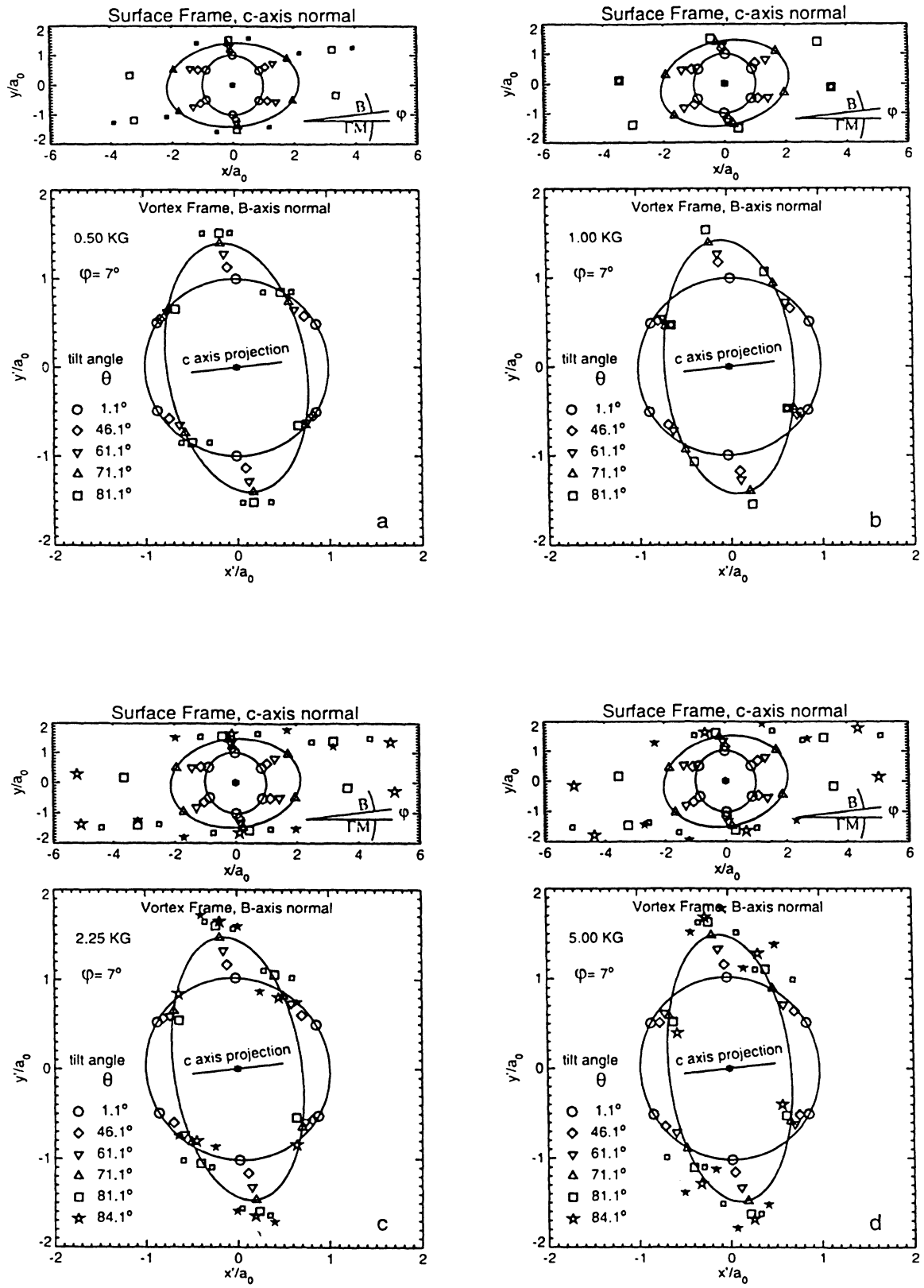


FIG. 4. Vortex basis vectors normalized to $a_0$ as observed in the surface frame (top) and transformed to the vortex frame (bottom) at different field magnitudes at angles indicated by symbols in the lower left of each subfigure. The averaged basis vectors, large symbols, lie on an ellipse ($\theta=1.1°$ and $\theta=71.1°$ are shown), which becomes increasingly elongated with larger $q$. At the highest angles (81.1° and 84.1°) the buckling instability results in a more complex unit cell. Here smaller symbols show a pair of vortex basis vectors shifted to the left and right of the average basis vector. This is for the $\varphi=7°$ field projection.

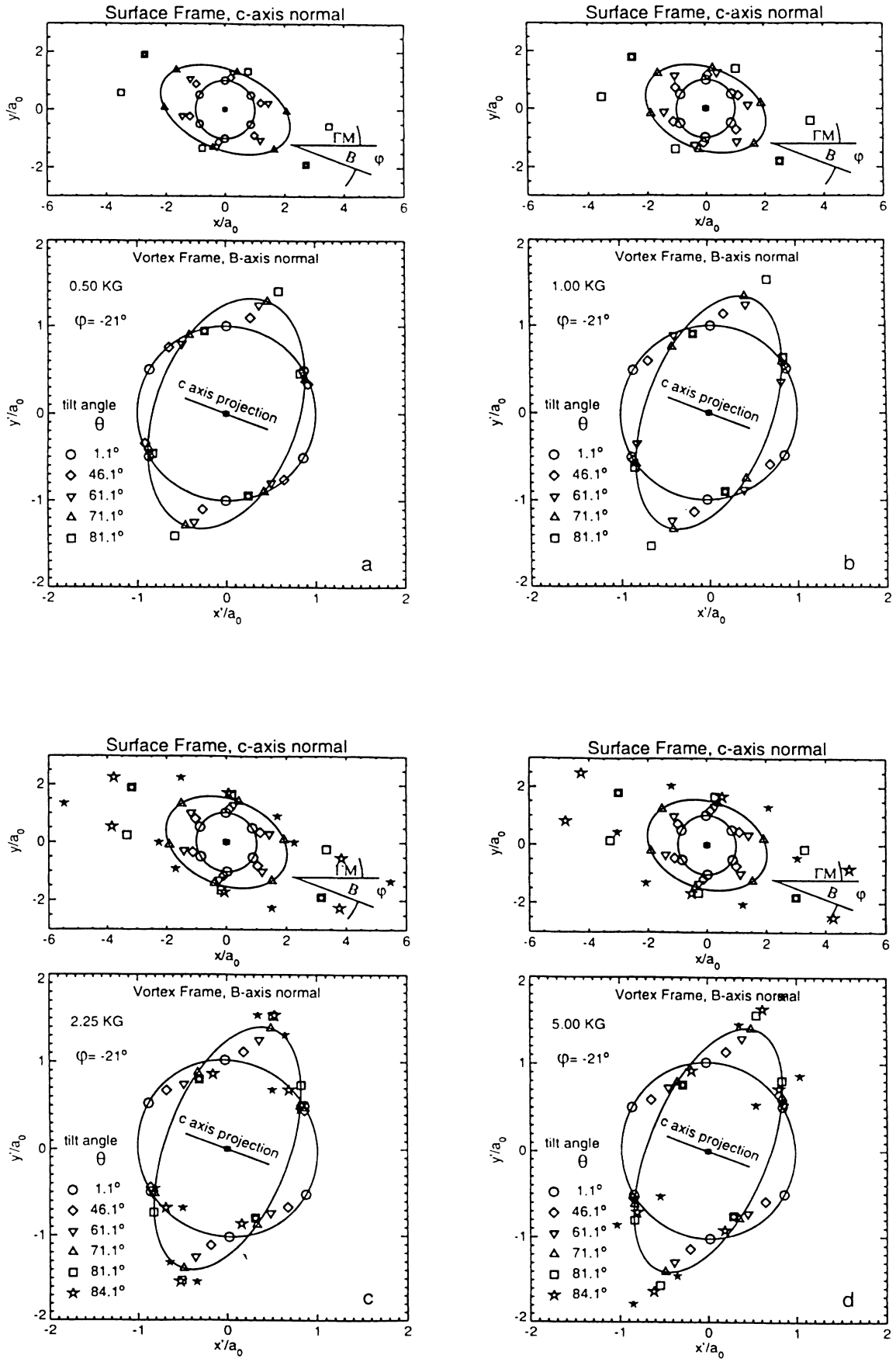


FIG. 5. Same as Fig. 4 except the $\varphi = -21°$ projection is presented.

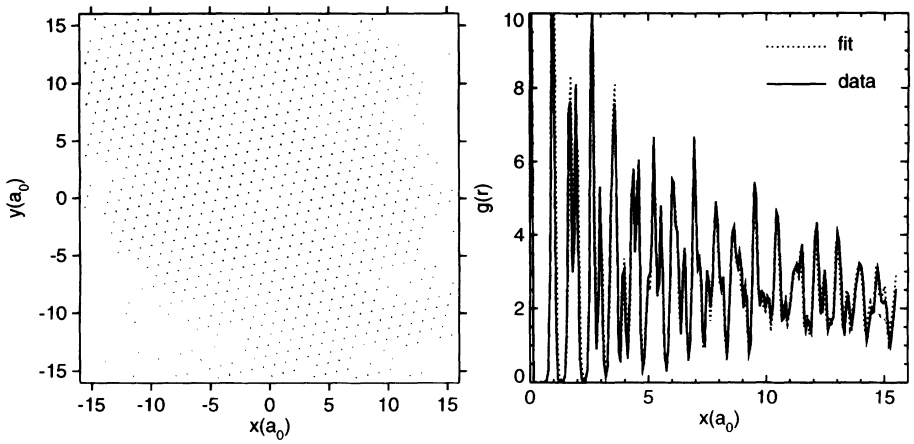


FIG. 6. Two-dimensional real-space correlation function at 5000 G and $\theta = 1.1°$ and its corresponding radial correlation function.

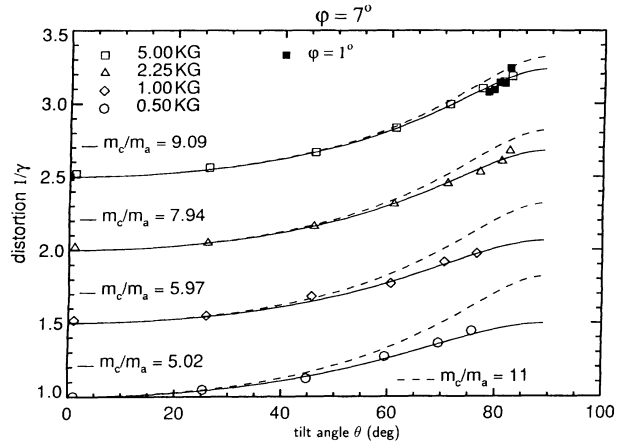


FIG. 7. Normalized semimajor axis length $1/\gamma$ that describes the lattice distortion in the vortex frames of the data shown in Fig. 2. The lines indicate predictions of anisotropic London theory for various mass ratios as indicated. Lower fields systematically show a more "isotropic" behavior with lower fitted values for the mass ratio, with the best fit depicted by the dashed lines. Here the $\varphi = 7°$ field projection corresponding to Fig. 4 is shown.

rearrangement of the vortices as they approach the surface at these high fields.

At lower fields there are field-dependent corrections to $1/\gamma$. If this data is also compared with Eq. (3), the best fit requires a smaller value of $m_c/m_a$ (Fig. 9). Also, decoration experiments[14] at much lower fields $a_0/\lambda \sim 3$ show a simple $\cos(\theta)$ dependence on the surface frame which would be consistent with an inferred mass ratio of 1. This trend of smaller ellipticity at smaller fields agrees with a more "isotropic" deduced mass ratios at low fields. The deviation from bulk theories may arise from two possible reasons: the $a_0/\lambda \ll 1$ approximation is no longer valid and higher-order terms of $a_0/\lambda$ must be included in the expansion modifying the form of Eq. (3); or competing surface monopole interactions[19] at the ends of the flux lines may begin to dominate the bulk behavior. This interaction would be relatively stronger at lower fields and would also encourage a more isotropic behavior.

## ANGLE OF BASIS VECTORS ON THE ELLIPSE

The angular orientation of the vortices on the ellipse can also be compared to theory. Here there is clear disagreement between experiment and the predicted

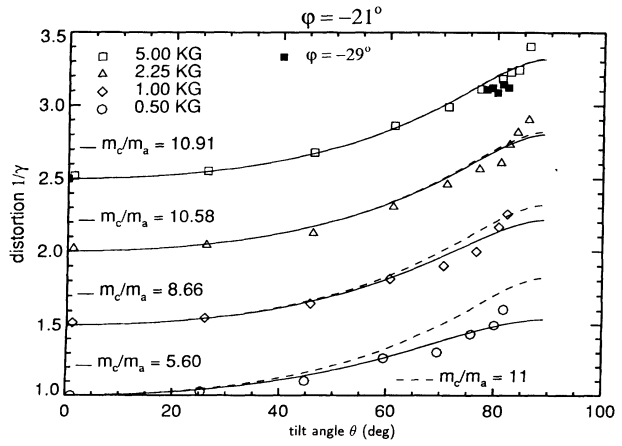


FIG. 8. Same as Fig. 7 except the $\varphi = -21°$ projection is presented.

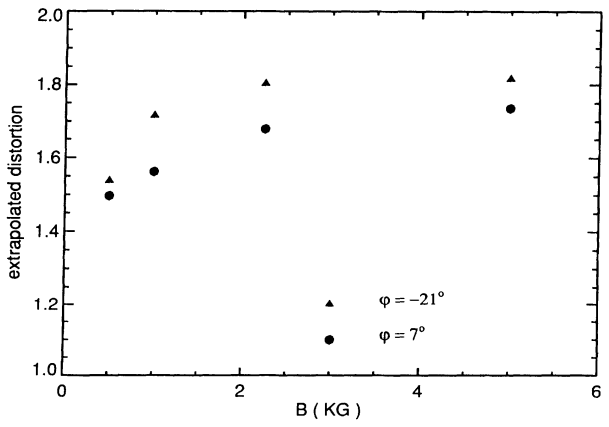


FIG. 9. Distortion in the vortex frame extrapolated to 90° vs $B$ for the data in Figs. 5 and 6.

lowest free-energy lattice orientation. As the tilt angle increases we see two of the vortex basis vectors align with the semimajor axis, in the vortex frame, perpendicular to the tilt direction. This is at odds with both the Landau-Ginzberg[9] and London[8] model theory, where a fourth-order term in the free-energy expansion predicts an alignment along the semiminor axis (parallel to the tilt direction), commonly referred to as vortex chains. The 30° deviation from prediction has also been confirmed in two other recent experiments on $2H$-$NbSe_2$: neutron scattering[13] (at $\varphi=0°$), which confirms agreement with bulk behavior and Bitter decoration,[14] which extends this observation to much lower fields and is also probing the surface. One might suspect that the in-plane crystalline anisotropy may play a role and prevent vortex chain formation, since it certainly defines the orientation for normal fields. We test this by tilting in two different planar directions $\varphi=7°$ and $-21°$, where the effect of crystalline anisotropy should be quite different. We find that, both cases show the same limiting behavior as the field is inclined toward the plane. One might also ask, is there partial locking to the crystal lattice? In other words, do any of the basis vectors remain at 30° to the six $\Gamma M$ directions? This might be the case for $\varphi=7°$ where four of the six basis vectors at 12, 2, 6, and 8 o'clock roughly retain the same angle (see Fig. 2 surface frame). This may not be so surprising since the $\varphi=0°$ tilt projection is the energetically favored projection where the in-plane atomic crystalline induced flux basis angles are in about the same direction as that induced by the out-of-plane anisotropy from the tilted magnetic field.

The same cannot be said of the $\varphi=-21°$ data where all of the basis vectors rotate clockwise as the tilt angle increases. For example two of the basis vectors rotate toward the preferred semimajor axis direction of the ellipse in the vortex frame. In the most frustrated case at $\varphi=30°$ the rotation could turn in either a clockwise or counterclockwise direction to reduce energy. How quickly this reorientation takes place as a function of angle can best be seen in Fig. 5(d) (vortex frame), where a solid line highlights the trajectory of one of the basis vectors as it swings out to align itself with the ellipse semimajor axis as $\theta$ increases. This appears to take place gradually and continuously between $\theta=0°$ and 70° with no significant differences observed at lower field magnitudes. At the considerably lower fields of decoration experiments,[14] vortices can be so far apart that the flux lattice basis vectors no longer lock to the atomic crystalline lattice for $\theta=0°$. Then the field tilting results in a similar gradual realignment of the basis vectors along specific tilt determined directions as angular order is induced. Therefore, the crystalline in-plane anisotropy does not appear to be the reason why the observed orientation of the real flux-line lattice differs from the model predictions.

Finally, is it fair to compare the data with the Landau-Ginzberg limit? After all, the data set was field cooled to 0.2 K where $T/T_c \sim 0$, while the Landau-Ginzberg model should be good only close to $T_c$. A study of a 70° inclined lattice was performed at different temperatures to address this question. For $\varphi=5°$ at $T=0.1$, 5, 5.5, and 6 K, there was no discernible change in the vortex locations. At higher temperatures contrast is lost and it becomes difficult to identify the vortex location. The lack of temperature sensitivity suggests that the low-temperature data accurately describes all basis vectors up to about $0.9T_c$.

## LARGE TILT ANGLE BEHAVIOR

At tilt angles larger than 78° away from the $c$ axis the configuration of the flux-line lattice becomes more complicated. In the STM data (Fig. 2) one observes that originally straight rows of vortices at 77.1° (aligned perpendicular to the tilt direction) become buckled with varying periodicities at larger angles. At $\varphi=7°$, $B=2.25$ kG for instance, one sees a progression from straight rows at 77.1° to a $3\times1$ reconstruction at 81.1° to a $2\times1$ reconstruction at 84.1°. These new basis vectors are also shown with somewhat smaller symbols (squares and stars) in Fig. 4 surrounding the larger symbol of their weighted average.

A sequence of STM data that explores this progression in more detail is shown in Fig. 10 at $B=5.00$ kG at $\varphi=1.5°$ and 28.5°. These vortex images have already been corrected for the STM distortions and rotated so that two of the $\Gamma M$ directions are essentially horizontal. Deviations from straight rows of vortices begin at tilt angles greater than 80° for both the $\varphi=1.5°$ and 28.5° data. The amplitude of the wiggles, which form mostly a $2\times1$ pattern, increases smoothly as the field is tilted further into the plane. Shear or long-wavelength transverse distortions at $k=0$ can be identified when the rows of vortices are no longer aligned normal to the **Bc** plane. The same data is shown as a real-space correlation function in surface coordinates in the adjacent columns. Here we observe the well-defined spot of the nearest-neighbor vector along the rows at 78.3° broadens into an arc at 80.3°. By 82.3° this arc extends further and begins to lose amplitude in the center, so that by 84.3° it splits into two arcs. The other nearest-neighbor vectors generally also experience some elongation in their distribution, although sometimes one pair can remain well defined, e.g., 80.3° and 81.3° at $\varphi=1.5°$. Finally disorder becomes most pronounced at the highest tilt angles. The data of Fig. 2 also shows that the threshold for these instabilities occurs at slightly smaller tilt angles (by a few degrees) for lower magnetic field.

Currently, the buckling at higher tilt angles has not been explored by other experiments in $2H$-$NbSe_2$ and an open question remains whether this is purely a surface phenomenon or is also manifested in the bulk. Recently, several theories[20–23] have addressed this issue of higher-order lattice structures in bulk vortex lattices mostly for the more highly anisotropic high-$T_c$ superconductors. Yet so far, a quantitative prediction for the mass ratio, fields, and angles of this sample has not been made. It is tempting to speculate that the buckling and other associated reconstruction is driven by the monopole interactions of the vortex ends as they penetrate the surface. Indeed the repulsive monopolar interactions, which should be isotropic on the surface, could create an enhanced surface energy for the straight rows that are

observed at 79°. The repulsive force between vortices in each row could be relieved if the spacing of vortices in a row were allowed to increase such as by some buckling distortion. The amplitude of buckling would be limited by the restoring force of bending the vortices close to the surface.

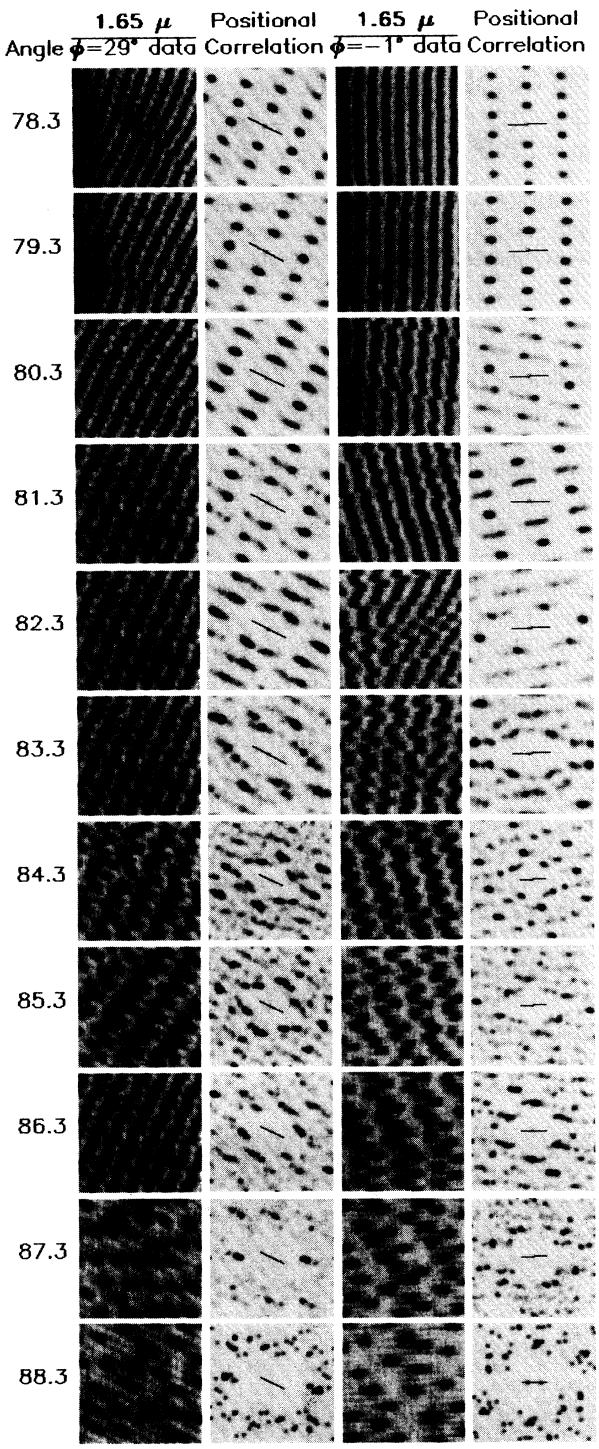


FIG. 10. STM data showing vortex lattice at shallow tilt angles for two different in-plane projections $\varphi=-28.5°$ and $\varphi=1.5°$. The two adjacent columns show the positional correlation functions of the same data. The line going through the center of these images indicates the direction of the field projected on the surface and its length defines a distance of 0.3 $\mu$m.

## INCLINED VORTEX CORE SHAPE

There have been suggestions that the vortex lattice structure can be strongly influenced by the shape of the vortex core, such as elliptical cores created by anisotropic coherence lengths. The shape of the core itself can also reflect variations of the superconductivity across the Fermi surface. Furthermore, the structure of an inclined vortex at the surface has never been probed. The STM is the ideal tool to probe this and has been effective previously[17] for imaging perpendicular vortices in 2H-$NbSe_2$. Conductance images of $dI/dV(x,y)|_V$, with a tip sample voltage of $V$ were taken at 100 mK with an ac dither voltage of 30 $\mu$V. They show directly the spatial shape of the vortex core wave functions with an energy of $eV$. If $eV$ is less than $\Delta_0$, then the imaged states are bound in the potential well formed by a spatially varying gap that collapses on the axis of the flux line. These states can be described by solutions of the Bogoliubov equations[24–26] or Eilenberger equations.[27] The lowest-energy bound states are imaged at $V=0$ at the Fermi energy. If the field is normal to the surface the vortex states exhibit a star shape, Fig. 11(a). The size scale of this core state should be set by a radial decay length of order the superconducting coherence length $\xi$. The six rays of the star can be interpreted as directions in which the gap does not recover away from the core (in other words the coherence length diverges). This is caused by local Fermi surface anomalies in those directions, specifically the charge-density wave (CDW) gap, which coexists with the superconducting gap. Double subgap structures of the energy spectrum near the core indicate that two parts of the Fermi surface contribute:[17] one which is in-plane angle independent and one which has six rays forming angle-dependent divergences in the plane (from the CDW gap). The two parts might be distinguished by different height, $k_z$, on the Fermi surface.

For tilted fields at $\theta=80°$, Fig. 11(b), a rather different cometlike structure is observed. The rays to the left side have been suppressed and those to the right, where the flux line penetrates horizontally beneath the surface at $\varphi=1.5°$ remain. To describe this shape may require more than assuming the vortex penetrates the surface at an angle, in addition there is also a uniform surface current sheath flowing vertically. The total local current from the sheath and the vortex superimpose and tend to add on the right side and cancel on the left. This would suppress superconductivity preferentially on the left. Figure 10(c) shows the energy evolution of a vortex core state tilted at $\theta=70°$ and $\varphi=28.5°$ at the indicated energies. Here one observes seven rays with the ones on the left being suppressed. The new separate seventh ray is visible on the surface above the buried flux line and radiates to the right, halfway between a pair of the original six rays.

In Fig. 12 the complete energy evolution of a $\theta=0°$, 70°, and 80° vortex at $\varphi=28.5°$ is presented. At $\theta=0°$ the energy evolution of each star is described by each of the

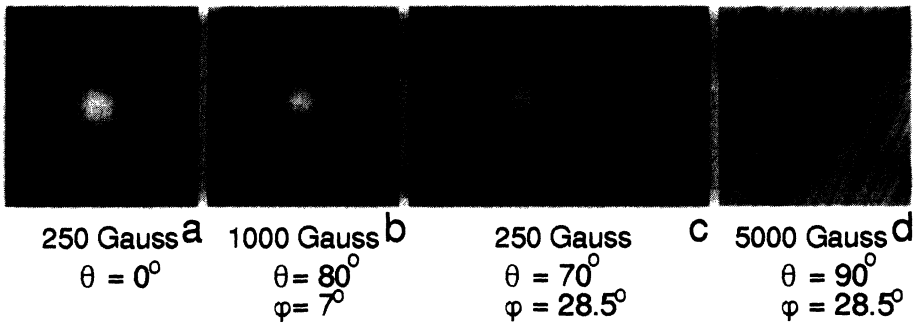


FIG. 11. Vortex core conductance images at the Fermi level $eV=0$ at 250 G over a 0.16-$\mu$m-sized box for (a) and (c). (a) $\theta=0°$ applied field, (b) $\theta=80°$ at $\varphi=7°$ over a 0.15-$\mu$m-sized box, (c) $\theta=70°$ at $\varphi=-28.5°$, (d) $\theta=90°$ at $\varphi=-28.5°$, and $B=1000$ G imaging the scattering states at 1.0 meV over a 1.65-$\mu$m-sized region showing evenly spaced stripes observed when the field is applied parallel to the surface.

six rays splitting into a pair of parallel lines, where the spacing between the pair scales monotonically with energy. This gives a rather intricate evolution[28] of the flux lattice images. A perturbative solution[29] to the Bogoliubov-de Gennes equations gave some insight into these various patterns, but many of the striking details, such as the split rays, need a more complete theory. For tilted vortices the same trends are visible except one must include the seventh ray. This feature broadens and intensifies with higher energies and develops into a sideways V shape. The opening angle of the V increases with energy and evolves into the sideways U core structure at the highest energies that approach $\Delta_0$. The physical origin and significance of this seventh ray and its splitting into a V is not understood.

Related structure is also visible in the scattering states, in other words, images that have been made at $eV>\Delta_0$ at $V=1.1$ mV. The data taken at the shallowest angles in Figs. 2, 10, and 11 tend to show streaks oriented along the field direction and often terminating in a vortex. This data also shows a dependence of the core shape on the in-plane angle, $\varphi$. For $\varphi=28.5°$ double cometlike tails are associated with each core. This contrasts with the behavior at $\varphi=1.5°$ where triplet tails are observed. If the field is turned very close to $\theta=90°$ the number of vortices drops and mainly long streaks or depressions in the conductance are visible in Fig. 11(d). Different magnetic-field images show that the streak separation scales with 1.55 $a_0$ and may reflect the spacing of subsurface vortices. If we assume the vortex rows remain aligned normal to the **Bc** plane, then the spacing normalized by $a_0$ should be a measure of $1/\gamma$ at $\theta=90°$. This value ($1/\gamma=1.55$) is significantly lower than the extrapolated values of $1/\gamma$ plotted in Fig. 9 at $\theta=90°$. If the lines reflect the subsurface vortex spacing, the cause of the reduced separation may be the surface boundary condition. Vortices close to and parallel to the surface interact not only with other vortices further into the bulk, but also with the surface current sheath and opposite polarity image vortices above the surface. This could produce a vortex configuration or a density different from that assumed in the bulk. At 90° neutron-scattering confirms a lattice consistent with the elliptical distortion of the anisotropic mass theories, despite some broadening of the diffraction spots.[13] This suggests that surface and bulk lattices may be different in the 90° case or possibly that the lines are not a good indicator of surface vortex spacing.

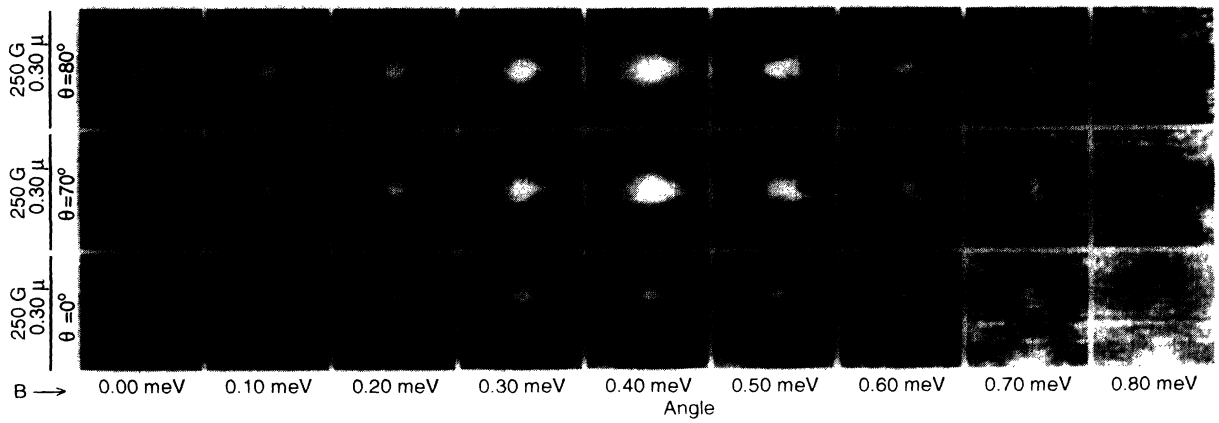


FIG. 12. Grey scale image of the conductance pattern $dI/dV(x,y)|_V$ for an inclined vortex at $\theta=0°$, 70°, and 80° measured with different tip-sample dc voltages, showing the shape and size of the vortex core states of different energy.

Incidently Fig. 11(d) reveals also a hint of vortex motion. the vortex core in the lower center appears multiple times as a cut off round spot. Since the raster scan proceeds from bottom to top over the course of 2 h, it suggests that this vortex has moved up and to the left along the tilt direction discontinuously twice during the scan. Motion of the vortex surface penetration point along the field inclination direction (parallel to the lines) appears much less constrained by other vortices than lateral motion.

## CONCLUSIONS

We summarize the results on flux-line lattice structure in 2H-NbSe$_2$ with a phase diagram, Fig. 13. The shaded region indicates the range over which the data was taken. This range bridges the recent low-field decoration data[14] between 10 and 100 G and the higher-field neutron-scattering data[13] taken at 8000 G. For normal fields of 30–8000 G, the flux-line lattice is observed to lock orientationally to the atomic lattice. At moderate tilt angles the vortex basis vectors lie on an ellipse whose orientation is set by the direction of the field inclination. The ellipticity is set by the mass ratio and described by the London model at high fields $\sim 5$ kG and behaves more isotropically [i.e., surface normalized semimajor axis is given by $1/\cos(\theta)$] at low fields $\sim 10$ G. Contour lines of constant distortion fitted to the observed values of both the STM and neutron data show this trend from anisotropic to isotropic behavior as the field is reduced and $a_0/\lambda$ becomes unity or larger. The position of the vectors on this ellipse sweeps continuously away from the in-plane crystal locked position to one locked onto the axis of the tilt rotation as $\theta$ increases toward 80°. The same orientation of the basis vectors is observed in all 2H-NbSe$_2$ experiments for large tilt angles in both high- and low-field magnitudes and is at odds with bulk anisotropic theories. Beyond 80° inclination, shear and buckling instabilities are observed that are higher-order reconstructions initially, such as $3\times1$, and then tend to be dominated by $2\times1$ patterns as the tilt angle is increased. The amplitude of these wiggles also increases with tilt, until positional order of the surface penetrating vortices is lost close to 90°. At 90° evenly spaced parallel strips on the surface may give a new side view of the subsurface vortex order.

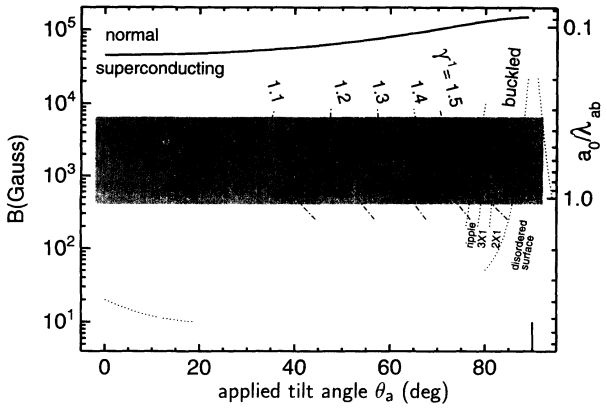


FIG. 13. $B$-$\theta$ phase diagram summarizing the contours of constant elliptical distortion and demarking the regions of different flux structures. The shaded region indicates the range over which the STM data was collected.

While some of the predictions of anisotropic theories are confirmed with these measurements in 2H-NbSe$_2$, other predictions, specifically those associated with angular orientation of the flux lines, need to be investigated. Possibly a more detailed description of the Fermi surface than the effective-mass approximation might be required for a full understanding. Clues of the relevance of the Fermi surface are already present in the unusual shape of the vortex core wave functions, their spectra, and their seventh ray for tilted conditions. The details of the vortex shape may be the key to a better characterization of the Fermi surface than the effective-mass approximation. The input of a more accurate Fermi surface into these lattice models may in turn be crucial, to resolving open issues in the flux lattice order.

## ACKNOWLEDGMENTS

The authors acknowledge useful discussions with V. Kogan, A. Yu Simonov, A. Sudbo, D. Huse, and R. Kleiman, and thank D. Grier for the data analysis code.

[1]L. Dobrosavljevic and H. Raffy, Phys. Status Solidi (B) **64**, 229 (1974).

[2]K. Takanaka, in *Anisotropy Effects in Type II Superconductors,* edited by H. W. Weber (Plenum, New York, 1977), p. 93.

[3]J. Schelten, G. Lippman, and H. Ullmaier, J. Low Temp. Phys. **14**, 213 (1974).

[4]G. J. Dolan, F. Holtzberg, C. Field, and T. R. Danger, Phys. Rev. Lett. **62**, 2184 (1989).

[5]A. M. Grishin, A. Yu Martynovich, and S. V. Yampol'skii, Zh. Eksp. Teor. Fiz. **97**, 1930 (1990) [Sov. Phys. JETP **70**, 1089 (1990)]; A. I. Buzdin and A. Yu Simonov, Pis'ma Zh. Eksp. Teor. Fiz. **51**, 168 (1990) [JETP Lett. **51**, 191 (1990)].

[6]C. A. Bolle, P. L. Gammel, D. G. Grier, C. A. Murray, D. J. Bishop, D. M. Mitzi, and A. Kapitulnik, Phys. Rev. Lett. **66**, 112 (1991).

[7]P. L. Gammel, D. J. Bishop, J. P. Rice, and D. M. Ginzberg, Phys. Rev. Lett. **68**, 3343 (1992).

[8]L. J. Campbell, M. M. Doria, and V. G. Kogan, Phys. Rev. B **38**, 2439 (1988); L. N. Bulaevskii, M. Ledvij, and V. G. Kogan, *ibid.* **46**, 366 (1992).

[9]K. G. Petzinger and G. A. Warren, Phys. Rev. B **42**, 2023 (1990).

[10]For high-$T_c$ compounds, see, E. M. Forgan, Physica (Amsterdam) **185-189C**, 247 (1991); M. Yethiraj, H. A. Mook, G. D. Wignall, R. Cubitt, E. M. Forgan, D. N. Paul, and T. Armstrong, Phys. Rev. Lett. **70**, 857 (1993); B. Keimer, F. Dogan, I. A. Aksay, R. W. Erwin, J. W. Lynn, and M. Sarikaya, Science **262**, 83 (1993).

[11]For $UPt_3$, see, R. N. Kleiman *et al.*, Phys. Rev. Lett. **69**, 3120 (1992).
[12]H. F. Hess, C. A. Murray, and J. V. Waszczak, Phys. Rev. Lett. **69**, 2138 (1992).
[13]P. L. Gammel *et al.*, Phys. Rev. Lett. **72**, 278 (1994).
[14]C. A. Bolle, F. De La Cruz, P. L. Gammel, J. V. Waszczak, and D. J. Bishop, Phys. Rev. Lett. **71**, 4039 (1993).
[15]P. de Trey, S. Gygax, and J. P. Jan, J. Low Temp. Phys. **11**, 421 (1973).
[16]K. Takita and K. Masuda, J. Low Temp. Phys. **58**, 127 (1984); L. P. Le *et al.*, Physica (Amsterdam) **185-189C**, 2715 (1991).
[17]H. F. Hess, Physica (Amsterdam) **169B**, 422 (1991); in *Scanning Tunneling Microscopy,* Methods of Experimental Physics Series Vol. 27, edited by J. Stroscio (Academic, New York, 1993), p. 427.
[18]A. I. Buzdin and A. Yu Simonov, Physica (Amsterdam) **175C**, 143 (1991).
[19]V. G. Kogan, A. Yu Simonov, and M. Ledvij, Phys. Rev. B **48**, 392 (1993).
[20]A. Sudbo, E. H. Brandt, and D. A. Huse, Phys. Rev. Lett. **71**, 1451 (1993).
[21]L. L. Daemon, L. J. Campbell, A. Yu Simonov, and V. G. Kogan, Phys. Rev. Lett. **70**, 2948 (1993).
[22]S. T. Chui, Solid State Commun. **83**, 411 (1992).
[23]B. I. Ivlev and L. J. Campbell, Phys. Rev. B **47**, 14 514 (1993).
[24]C. Caroli, P. G. de Gennes, and J. Matricon, Phys. Lett. **9**, 307 (1964); C. Caroli and J. Matricon, Phys. Kondens. Mater. **3**, 380 (1965).
[25]J. Shore, M. Huang, A. T. Dorsey, and J. P. Sethna, Phys. Rev. Lett. **62**, 3089 (1989).
[26]F. Gygi and M. Schluter, Phys. Rev. B **43**, 7609 (1991).
[27]U. Klein, Phys. Rev. B **41**, 4819 (1990).
[28]H. F. Hess, Physica C **185-189**, 259 (1991).
[29]F. Gygi and M. Schluter, Phys. Rev. Lett. **65**, 1820 (1990).

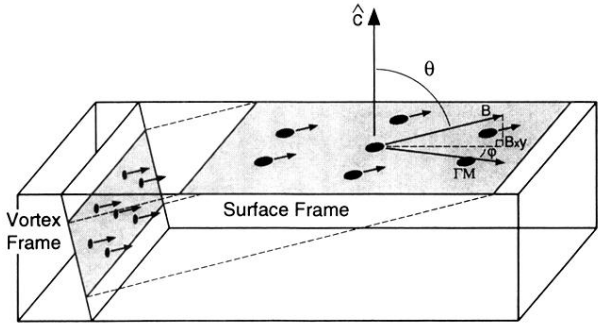


FIG. 1. Schematic detail of the direction of the magnetic field, the crystalline orientation, the scanned surface and the plane of the vortex basis vectors.

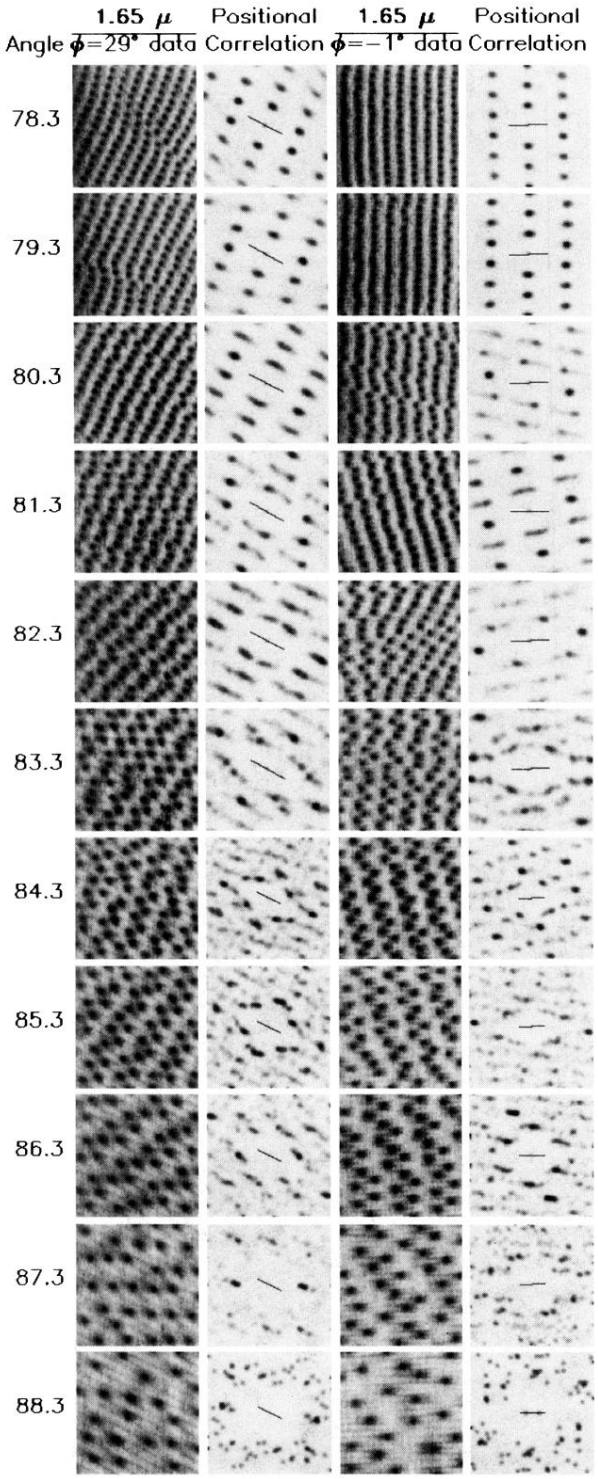


FIG. 10. STM data showing vortex lattice at shallow tilt angles for two different in-plane projections $\varphi = -28.5°$ and $\varphi = 1.5°$. The two adjacent columns show the positional correlation functions of the same data. The line going through the center of these images indicates the direction of the field projected on the surface and its length defines a distance of 0.3 $\mu$m.

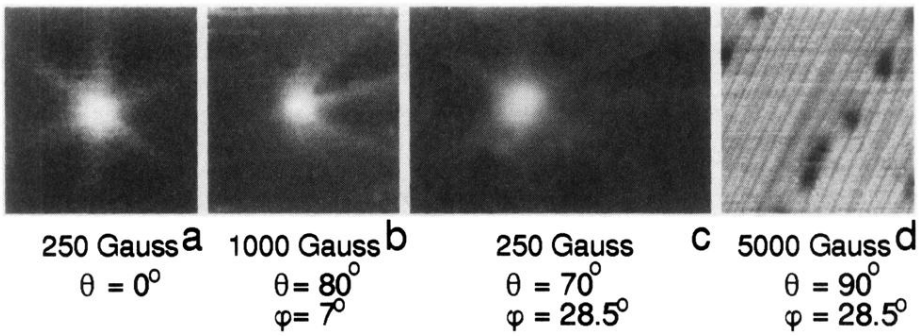


FIG. 11. Vortex core conductance images at the Fermi level $eV=0$ at 250 G over a 0.16-$\mu$m-sized box for (a) and (c). (a) $\theta=0°$ applied field, (b) $\theta=80°$ at $\varphi=7°$ over a 0.15-$\mu$m-sized box, (c) $\theta=70°$ at $\varphi=-28.5°$, (d) $\theta=90°$ at $\varphi=-28.5°$, and $B=1000$ G imaging the scattering states at 1.0 meV over a 1.65-$\mu$m-sized region showing evenly spaced stripes observed when the field is applied parallel to the surface.

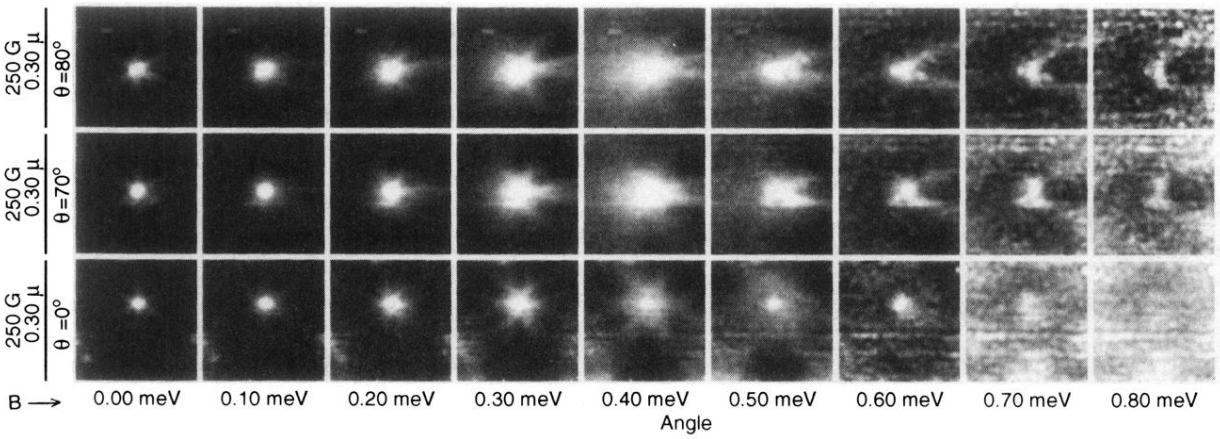


FIG. 12. Grey scale image of the conductance pattern $dI/dV(x,y)|_V$ for an inclined vortex at $\theta=0°$, 70°, and 80° measured with different tip-sample dc voltages, showing the shape and size of the vortex core states of different energy.

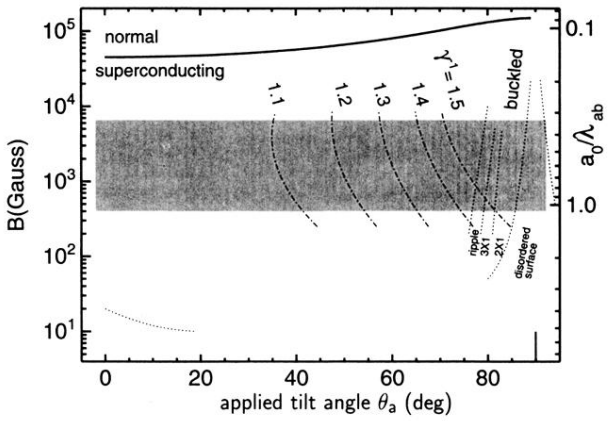


FIG. 13. $B$-$\theta$ phase diagram summarizing the contours of constant elliptical distortion and demarking the regions of different flux structures. The shaded region indicates the range over which the STM data was collected.

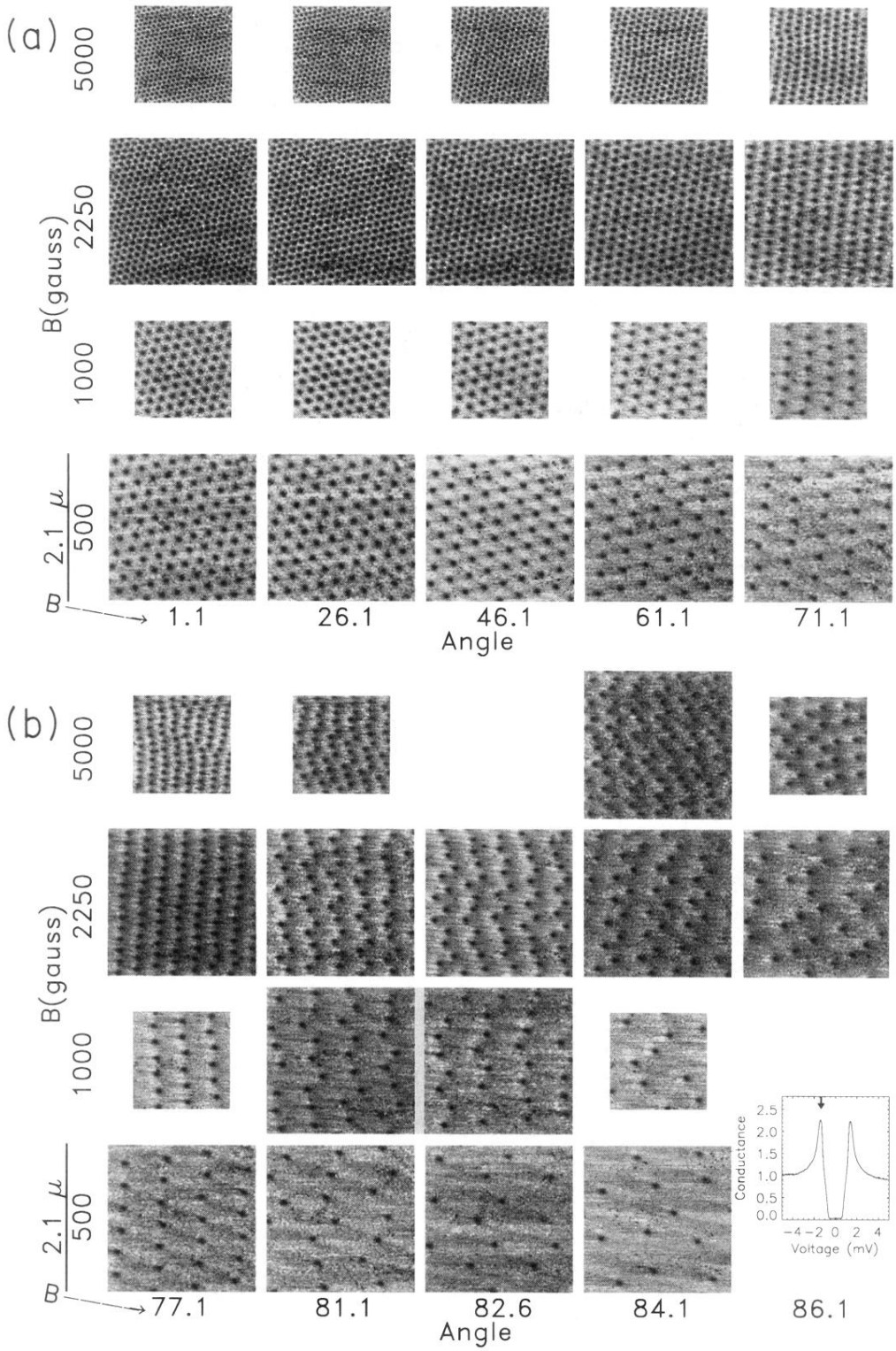


FIG. 2. Raw STM data showing on a grey scale the differential conductance $dI/dV(x,y)|_V$ at a dc voltage of 1.3 mV, just above the superconducting gap. (Zero-field spectrum is indicated in the inset.) The dark spots correspond to vortices where the differential conductance is reduced. Tilt angles, directions, and field magnitude are indicated.

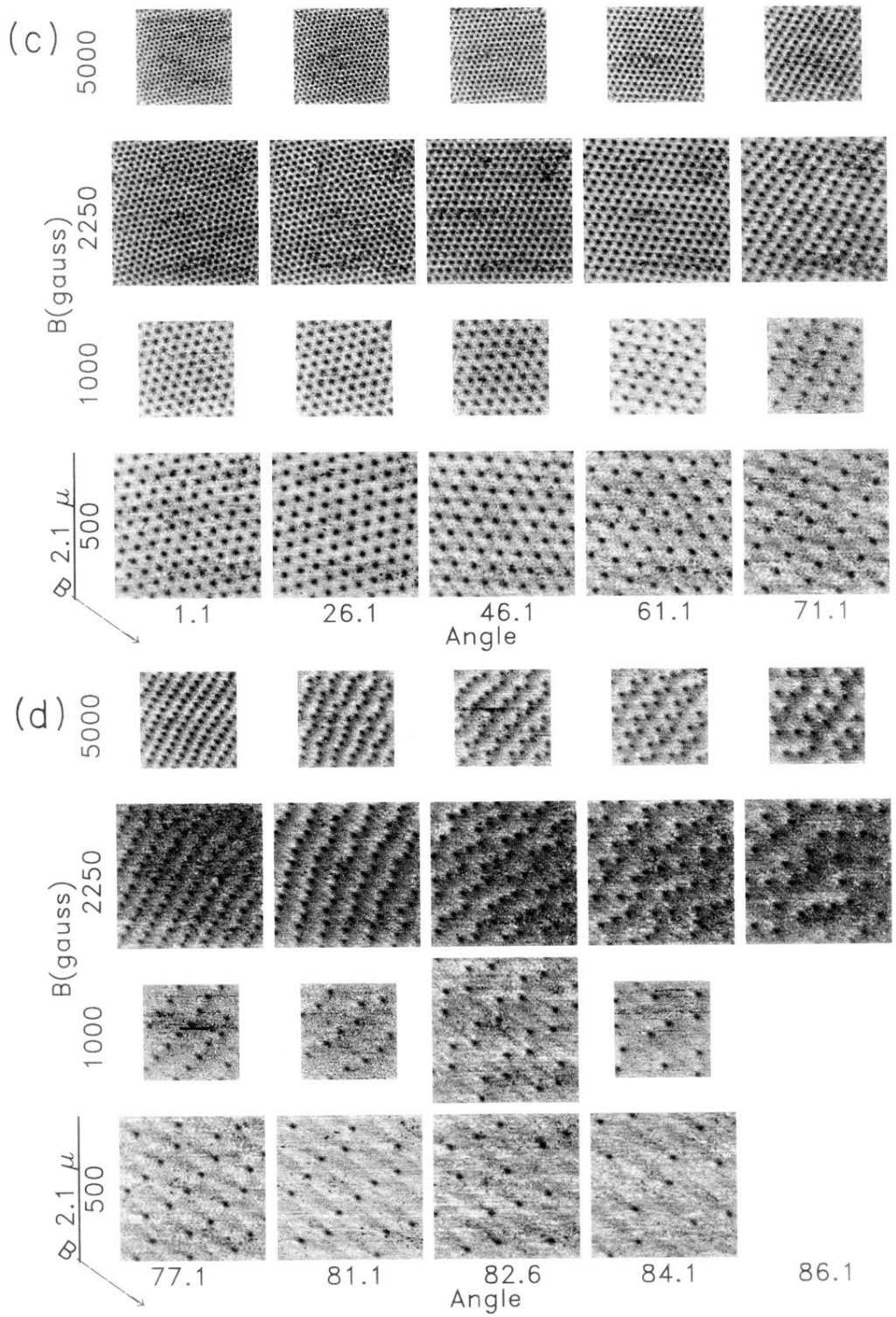


FIG. 2. (*Continued*).